Two-band modeling of α-prime phase formation in Fe-Cr

Pär Olsson,[1] Janne Wallenius,[1,2] Christophe Domain,[3] Kai Nordlund,[4] and Lorenzo Malerba[5]
[1]*Department of Neutron Research, Uppsala University, Uppsala, Sweden*
[2]*Department of Nuclear and Reactor Physics, Royal Institute of Technology, Stockholm, Sweden*
[3]*Department of Materials and Mechanics of Components, EDF R&D, Moret sur Loing, France*
[4]*Accelerator Laboratory, University of Helsinki, Helsinki, Finland*
[5]*Reactor Materials Research Unit, SCK-CEN, Mol, Belgium*
(Received 8 August 2005; revised manuscript received 25 October 2005; published 21 December 2005)

We have developed a two-band model of Fe-Cr, fitted to properties of the ferromagnetic alloy. Fitting many-body functionals to the calculated mixing enthalpy of the alloy and the mixed interstitial binding energy in iron, our potential reproduces changes in sign of the formation energy as a function of Cr concentration. When applied in kinetic Monte Carlo simulations, the potential correctly predicts decomposition of initially random Fe-Cr alloys into the α-prime phase as function of Cr concentration.

DOI: 10.1103/PhysRevB.72.214119 PACS number(s): 61.66.Dk, 61.80.Hg, 61.82.Bg

I. INTRODUCTION

The embedded atom method and second-moment tight-binding approximation many-body potentials have successfully been used to describe a number of physical properties of pure elements, including formation energies and mobilities of point defects.[1–3] When applied to alloys, Foiles and co-workers found that by fitting the ratio of *s*- and *d*-electron density, one could reproduce mixing energies that change sign as a function of alloy concentration, as is the case for Ni-Pd.[4] When including terms corresponding to *d*-electron density only, a strictly positive or negative heat of mixing results.[5–7] Hence, it appears that the small contribution of the *s*-band to the cohesive energy is essential for modeling of certain alloys. In a physically consistent picture, one should, however, consider that electronic structure calculations set limits to the variation of *s*-electron density. For 3*d* transition metals, one finds that the integrated density of *s*-states remains approximately constant at a value of about 1.5, while the *d*-band density increases with increasing average valence number. Therefore, it is rather the strength of *s*-band interaction that should be fitted, than the density *per se*.

In the original derivation of the second-moment tight-binding approximation to the many-body interaction, the repulsive force due to kinetic energy of *s*-band electrons was neglected.[8,9] Although the contribution to the total cohesive energy of the *s*-electrons is small, the opposite is true for pressure and especially elasticity.[10]

A better formulation of the embedded atom method is therefore needed, especially in the case of application to the Fe-Cr system, the basic component of ferritic-martensitic stainless steel. Fe-Cr forms a perfect ferromagnetic alloy for Cr concentrations up to 10% at $T=750$ K, but decomposes into two isomorphous phases, iron-rich α and chromium-rich α-prime, for Cr concentrations ranging from 10 to 90 at. %.[11–14] The size of the chromium-rich precipitates is on the nanometer scale, and the kinetics of the phase separation is faster under irradiation than under thermal aging.[15]

In this paper we construct a two-band (*s* and *d*) second-moment model that correctly describes the heat of mixing in Fe-Cr. The predictive capability of our potential is underlined by simulation of thermal aging, showing explicitly how the α-prime phase forms, either by spinodal decomposition or by nucleation and growth.

II. TWO-BAND MODEL OF TRANSITION METAL ALLOYS

A two-band model for Cs and other pure elements was recently suggested by Ackland.[16] Here, we apply the two-band approach in the Fe-Cr system. Extending Ackland's second-moment expression for the total energy of binary alloys with contributions from *s*-band electrons, we write for the energy of atom i (Refs. 5 and 17):

$$E_i = \frac{1}{2}\sum_j V(r_{ij}) + F_d(\rho_d) + F_s(\rho_s), \tag{1}$$

where $V(r_{ij})$ is the pairwise (electrostatic) interaction between core electrons of the atoms at site i and j, and $\rho_b = \Sigma\phi_b(r_{ij})$ represents the density of *s*- and *d*-band electrons yielding a many-body energy described by the functional $F_b(\rho_b)$. Note that the embedding functions for Fe and Cr are identical.

In line with Ackland, we write the band functional as

$$F_b(\rho_b) = A_1^b\sqrt{\rho_b} + A_2^b\rho_b^2 + A_3^b\rho_b^4, \tag{2}$$

where the coefficients A_i parametrize the relative strength of cohesive and repulsive forces.

In order to highlight the importance of the *s*-band contribution to the mixing enthalpy of the alloy, we present the following instructive example. Consider the case of a potential where the *d*-band yields a positive mixing enthalpy with a parabolic shape. For simplicity, assume equal density functions $\phi^{AB}(r)$ of first nearest-neighbor range and no contribution from the kinetic energy. The *d*-band mixing enthalpy as a function of solute concentration C_B may then be written in arbitrary units (a.u.) as

$$H_d^{\mathrm{mix}} = 1 - \sqrt{C_B^2 + C_B(1-C_B) + (1-C_B)^2}, \tag{3}$$

which has a maximum of 0.125 a.u. at $C_B=50\%$. Assuming that the impact of the *s*-band that we would like to catch is a

TABLE I. Spline coefficients and cutoffs for the Cr pair potential, electron-density function and band functional here used. Cutoffs are given in units of nearest-neighbor distance in Cr (2.4924 Å). The unit for the spline coefficients is electron volts per cubic angstroms.

i	1	2	3	4
r_i	0.976	1.150	1.216	1.650
a_i	−165.0	−78.49908	−78.15495	+1.8679553
r_k	0.963	1.284	1.685	
b_k	−11.0828	+0.013905	−0.447541	
A_i	−0.56479	-8.8959×10^{-4}	$+9.0265\times10^{-8}$	

perturbation in the mixing enthalpy, we may set $\phi_s^{AA}=\phi_s^{BB}=0$. Adding a cohesive energy of the s-band equal to

$$H_s^{\text{mix}} = -\sqrt{0.01C_B(1-C_B)}, \tag{4}$$

one finds minima in the formation energy at 1.0% concentration of solute atoms, having a magnitude of −0.005 a.u., comparing to the maximum at equal concentrations of 0.85 a.u. The relative magnitude of the extrema is in good agreement with actual calculations of the formation energy in transition metal alloys.[18] Hence, an increase in electron density of merely 1% due to s-band mixed-pair interaction should be sufficient to allow the present model to reproduce the concentration dependence of the formation energy calculated *ab initio*.

III. POTENTIALS FOR Fe AND Cr

The pair interaction and the many-body functionals for Fe were taken from the recent work of Ackland and Mendelev.[17] This potential provides values for self-interstitial formation energies in reasonable agreement with *ab initio* calculations and has therefore been applied to simulations of defect evolution.[19] To the special features of this potential belong a cohesive energy of 4.03 eV and a density function normalized to the total electron number of iron, which is 26. Consequently, the Cr potential previously developed by us,[7,20] may not be directly coupled with the Ackland-Mendelev potential for Fe. We have chosen to refit our Cr potential to yield a cohesive energy of 3.84 eV in order to retain the difference in cohesive energy between Fe and Cr. The density function for Cr has the same shape as the one used for Fe by Ackland and Mendelev, but is normalized to a total electron density of 24 at equilibrium. The following parametric form of the pair interaction is assumed:

$$V(r) = \sum_i a_i(r-r_i)^3 H(r_i-r). \tag{5}$$

Here, r_i are cutoffs of the cubic splines used to represent the potential, H is the Heaviside step function, and a_i are spline coefficients. Similarly, the density function of chromium is represented by

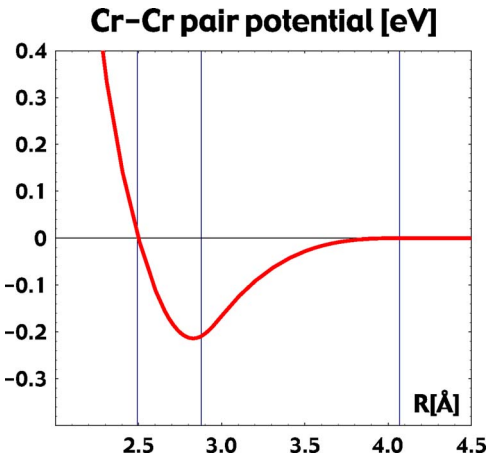

FIG. 1. (Color online) Pair interaction $V(r)$ for pure Cr. The vertical lines represent positions of first, second, and third nearest neighbors.

$$\phi_d^{\text{CrCr}}(r) = \sum_k b_k(r-r_k)^3 H(r_k-r). \tag{6}$$

The coefficients of the pair potential and the many-body functional (2) were fitted to the experimental lattice parameter at 0 K, the elastic constants of paramagnetic chromium extrapolated to 0 K and the relaxed formation energies for vacancies and self-interstitials calculated with Vienna Ab-initio Simulation Package (VASP) and the Projector Augmented Wave (PAW) algorithm.[21–23]

In Table I, the coefficients and cutoffs for Cr used in the present paper are given. Note that although the coefficient of the squared electron density in the band functional is negative, as is the case for the Fe potential by Ackland and Mendelev, our band functional has a second derivative that is positive everywhere.

In Figs. 1 and 2, the resulting pair potential and band functional are displayed. The properties of chromium calculated with the potential are compared to experimental and/or *ab initio* data in Table II. We include values for nonrelaxed ($E_{\text{vac}}^{\text{nr}}$) as well as relaxed ($E_{\text{vac}}^{\text{rel}}$) vacancy formation energies to highlight the fact that the relaxation energy observed in the

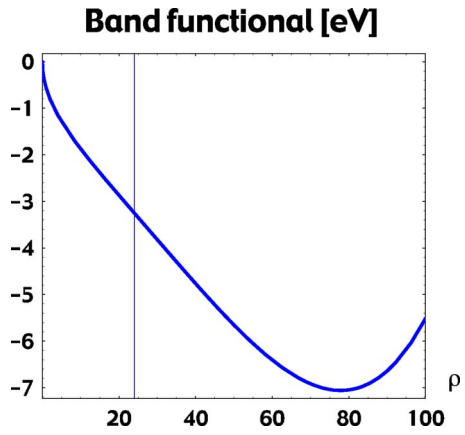

FIG. 2. (Color online) D-band functional $F_d(\rho)$ for pure Cr. The vertical line represents the equilibrium density.

TABLE II. Properties of Cr calculated with the present potential. Comparison is made to experimental data for paramagnetic Cr extrapolated to 0 K and VASP calculations for paramagnetic Cr in the PAW formalism.[23]

	This work	Experiment	VASP-PAW
a_0(Å)	2.878	2.878[a]	2.834
B(GPa)	208	208[b]	
C'(GPa)	152	152[b]	
C_{44}(GPa)	105	105[b]	
E_{coh}(eV)	3.84	4.10	
E^{nr}_{vac}(eV)	2.88		2.89
E^{rel}_{vac}(eV)	2.56	2.0±0.2[c]	2.59
E^{mig}_{vac}(eV)	0.99	0.95[d]	
$E_{fcc}-E_{bcc}$(eV)	0.03		
$E^f_{\langle 110\rangle}$(eV)	5.60		5.66
$E^f_{\langle 111\rangle}$(eV)	5.62		5.68
$E^f_{\langle 100\rangle}$(eV)	6.83		6.78

[a]Reference 24.
[b]Reference 25.
[c]Reference 26.
[d]Reference 27.

ab initio calculation is well reproduced by our potential.

IV. ALLOY POTENTIAL

In an alloy, one may expect that the electron density is dependent on the local environment. For the mixed-pair density we choose the square of a 4*s*-type Slater function

$$\phi_s^{FeCr}(r) = (N_s r^3 e^{-\zeta_s r})^2, \tag{7}$$

where $\zeta_s = 1.323$ is an average ζ from single ζ approximations of the 4*s* Hartree-Fock Fe and Cr orbitals,[28] providing a natural cutoff at 5.3 Å. $N_s = 5.0$ is chosen to yield an *s*-electron density at first nearest-neighbor distance equal to 2% of the corresponding *d*-electron density.

Our alloy potential should predict changes in the sign of the mixing enthalpy. *Ab initio* calculations made with the exact muffin-tin orbital method (EMTO)[18,29] indicate that this property is due to a minimum in the density of states at the Fermi level for a chromium concentration of 10 %. Furthermore, there is a small increase in the relative *s*-band density of the alloy as compared to that of a linear interpolation between the pure elements. We may, hence, contain the entire concentration dependence of this deviation in the mixed-pair density function ϕ_s^{FeCr}, setting ϕ_s^{FeFe} and ϕ_s^{CrCr} equal to zero.

First, we fit the mixed-pair potential to the lattice parameter of Fe-10Cr and a positive heat of mixing for equimolar composition.

Then, the coefficients of the *s*-band functional are fitted to the negative substition energy of a single Cr atom in bcc Fe and the crossing point from negative to positive mixing enthalpy, while constraining the second derivative of the *s*-band functional to be everywhere positive. For small concentrations, the term dependent on the square root will have a larger weight than terms quadratic and quartic in mixed density. The opposite is true for intermediate compositions.

TABLE III. Spline coefficients, cutoffs, and band coefficients for the Fe-Cr potentials are presented here. Cutoffs are given in units of 2.861 Å for Fe-Cr. The unit for the spline coefficients is electron volts per cubic angstrom.

i	1	2	3	4
r_i	0.970	1.15	1.40	2.14
a_i (VASP)	−47.3	−8.10	−7.82	+0.15
a_i (EMTO)	−67.0	−5.60	−8.40	+0.14
A^s_i (VASP)	−0.503	−0.60	+0.50	
A^s_i (EMTO)	−0.800	−1.00	+0.80	

Two sets of data were used for fitting of the substitution and mixing energies. One set[30] corresponds to data obtained with EMTO using the coherent potential approximation (CPA).[31,32] With this method, it is possible to perform calculations for arbitrary Cr concentrations, as the unit cell contains just one effective atom. The other set[23] is calculated with VASP in the PAW formalism, at a number of discrete Cr concentrations given by inserting an integer number of Cr atoms in a unit cell of different size.

Finally, the mixed-pair potential was fitted to the binding energy of the $\langle 110\rangle$ mixed dumbbell in bulk iron, which was calculated using VASP.

The molecular dynamics code DYMOKA[33] was revised to enable two-band functionals, and was extensively used during the fitting procedure. Table III displays coefficients fitted to the two sets of mixing enthalpy data. The mixing enthalpy was calculated as a function of Cr concentration in boxes with 16 000 randomly distributed atoms and is shown in Fig. 3. The interatomic potentials reproduce the *unrelaxed* mixing energy previously calculated with EMTO up to about 50% Cr concentration,[18] as well as the relaxed mixing energy ob-

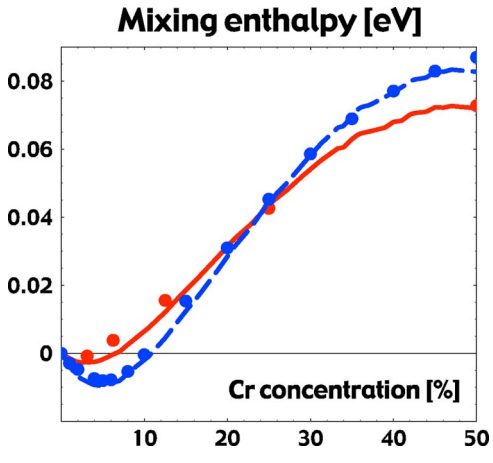

FIG. 3. (Color online) Mixing energy in random Fe-Cr alloys. Red circles: VASP mixing energy.[30] Blue circles: EMTO mixing energy.[30] Red solid line: relaxed MD mixing energy obtained with the potential fitted to VASP data. Dashed blue line: unrelaxed MD mixing energy obtained with the potential fitted to EMTO data.

TABLE IV. Substitutional and interstital energies of Cr atom(s) in an iron lattice. Potential A is fitted to the mixing enthalpy calculated with VASP, potential B to the mixing enthalpy calculated with EMTO. Comparison is made with 128 and 129 atom VASP-PAW calculations.[23] Energies are given in electron volts.

	Pot A	Pot B	VASP[23]
$E_{\text{sub}}^{\text{Cr}}$	−0.02	−0.27	−0.02
$E_{\langle 110\rangle}^{\text{Fe-Cr}} - E_{\langle 110\rangle}^{\text{Fe-Fe}} - E_{\text{sub}}^{\text{Cr}}$	−0.12	−0.13	−0.12
$E_{\langle 111\rangle}^{\text{Fe-Cr}} - E_{\langle 111\rangle}^{\text{Fe-Fe}} - E_{\text{sub}}^{\text{Cr}}$	−0.32	−0.38	−0.42
$E_{\langle 110\rangle}^{\text{Cr-Cr}} - E_{\langle 110\rangle}^{\text{Fe-Fe}} - 2E_{\text{sub}}^{\text{Cr}}$	+0.32	+0.46	+0.30
$E_{\langle 111\rangle}^{\text{Cr-Cr}} - E_{\langle 111\rangle}^{\text{Fe-Fe}} - 2E_{\text{sub}}^{\text{Cr}}$	+0.04	+0.24	−0.34

tained with VASP-PAW.

For higher concentrations, existing discrete Fourier transform (DFT) methods do not provide the negative substitution energy of Fe in Cr that may be expected from the existence of α-prime precipitates. This is most likely due to the alloy being spin-density wave antiferromagnetic for Fe concentrations up to 16% at 0 K,[34] a configuration that has not yet been successfully modeled within density-functional theory.[35] At room temperature, a Fe concentration of just 2% is sufficient to make the alloy paramagnetic. In order to be consistent with experiment, we have not made any effort to adjust the negative substitution energy of Fe in Cr resulting from our fitting procedure.

Table IV displays substitutional and interstitial properties of Cr in a Fe crystal obtained using the potentials fitted to the mixing enthalpy calculated with VASP (potential A) and EMTO (potential B). VASP *ab initio* data are provided as a reference. In the VASP calculation, PAW pseudopotentials with 300 eV cutoff energies were used within the general gradient approximation. The supercell size was 128 lattice sites, the number of k points was 27, and atoms of different configurations were relaxed at constant volume. It was found that the most stable interstitial configuration was the mixed $\langle 110\rangle$ dumbbell with a binding energy of 0.12 eV relative to the pure iron dumbbell.[23] Note that the mixed-pair potential was fitted to the binding energy of the mixed $\langle 110\rangle$ dumbbell, but not to the other configurations. We observe that the potential fitted to a smaller substitution energy (potential A) yields interstitial binding energies in better agreement with *ab initio* data. Potential B, which was fitted to EMTO mixing enthalpy, performs less well for Cr-Cr dumbbell binding energies.

V. SIMULATION OF THERMAL AGING

Using atomic kinetic Monte Carlo (AKMC) techniques, the time evolution of vacancy-driven thermal aging can be simulated in the alloy.

The AKMC simulation was performed with the LAKIMOCA code, based on the residence time algorithm.[36] A vacancy is introduced into the simulation box, and the kinetic Monte Carlo step consists of choosing one of the eight possible first-nearest vacancy jumps for a configuration according to their jump frequency Γ_k defined by

$$\Gamma_k^X = \nu e^{-\frac{E_{\text{mig}}^X + \Delta E/2}{kT}}, \tag{8}$$

where X is the the atom that jumps to the vacancy site and ν is the attempt frequency. The migration energies E_{mig} given by the presently used potentials are 0.65 eV for Fe and 0.52 eV for a single Cr atom in iron. ΔE is the energy difference of the system due to the vacancy jump, calculated using the potentials on on a rigid lattice (without relaxation). The average time step associated to the kinetic Monte Carlo step in a BCC lattice is

$$dt = \frac{1}{\sum_{k=1,8} \Gamma_k}. \tag{9}$$

As the vacancy concentration in the simulation box is much larger than under experimental conditions, the simulated time has to be rescaled in order to obtain the aging time. The scaling factor is the ratio between the vacancy concentration in the simulation box and the thermal equilibrium concentration $C_{\text{vac}}^{\text{eq}}(T) = e^{-G_f/kT}$, where G_f is Gibbs energy for the formation of a vacancy.

In our previous works, the alloy potential did not provide any change in sign of the formation energy, and hence, the decomposition at Cr concentrations above 10% was driven to complete segregation of the elements.[7] With the present potentials, however, we would expect that the segregation should remain incomplete. Hence, we performed AKMC calculations in $40\times40\times40$ lattice unit boxes for initially random distributions of Cr atoms in Fe-6Cr, Fe-8Cr, Fe-10Cr, and Fe-32Cr at $T=740$ K. In the case of Fe-32C, experimental information about the time dependence of the Cr distribution at this temperature exists.[12]

In the simulations with an initial Cr concentration of 6%, the alloy remained random up to a simulated time of one week. For 8% initial chromium content, the alloy remained random up to one week of simulated time using potential B (having a negative mixing enthalpy at this concentration). Applying potential A, having a positive mixing enthalpy at this concentration, weak clustering tendencies were observed.

In Fig. 4, the spatial Cr distributions in initially random Fe-10Cr and Fe-32Cr are exemplified in $40\times40\times10$ slices of the original box after 2×10^9 and 10^{10} vacancy jumps, corresponding to one week and one month of simulated aging, respectively. Potential A was used for the simulation displayed, but no qualitative difference is observed when switching to potential B in this range of concentration. One may compare these results to the experimental solubility limit at $T=670$ K, being 8.3%.[15]

Note that precipitate boundaries in Fe-10Cr are well defined, even for clusters located close to each other. Such geometries are typical for precipitate formation by nucleation, expected to occur where Gibbs' energy of formation has a positive curvature. Indeed, we observe that precipitates forming in Fe-10Cr are found at locations where the initial Cr concentration was slightly higher than the average due to random fluctuations. Furthermore, the size of the precipitates increase with time. In Fe-32Cr, the diffuse boundaries and

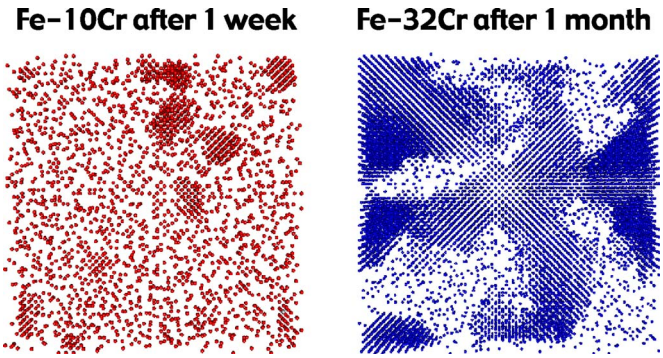

FIG. 4. (Color online) Cr distribution in initially random Fe-10Cr and Fe-32Cr aged at 740 K. The sharp precipitate boundaries found in Fe-10Cr are typical for nucleation processes, while the interconnected precipitates in Fe-32Cr result from spinodal decomposition. The potential fitted to VASP mixing enthalpy (potential A) was used in the simulation.

interconnected precipitates result from spinodal decomposition, corresponding to a negative curvature of Gibbs' energy.

Local Cr concentrations were calculated by taking the mean concentration in boxes with, on average, 45 atoms. The boxes were constructed analogously to the experimental method[12] and were sampled along the ⟨110⟩ direction. Figure 5 shows concentration profiles in Fe-10Cr and Fe-32Cr. Because of the method of sampling, the Cr concentration in the precipitates varies between 50 and 90%, consistent with the observation by Brenner *et al.*[12] For Fe-32Cr, we may compare the average size and distance of the precipitates in Fig. 4 to experimental data taken at 740 K, being 2 and 6 nm after 670 h of aging.[12] The cluster sizes and distances observed in our simulation are compatible with these data. To make a definite conclusion, a larger number of AKMC simulations would have to be done in order to provide statistical evidence.

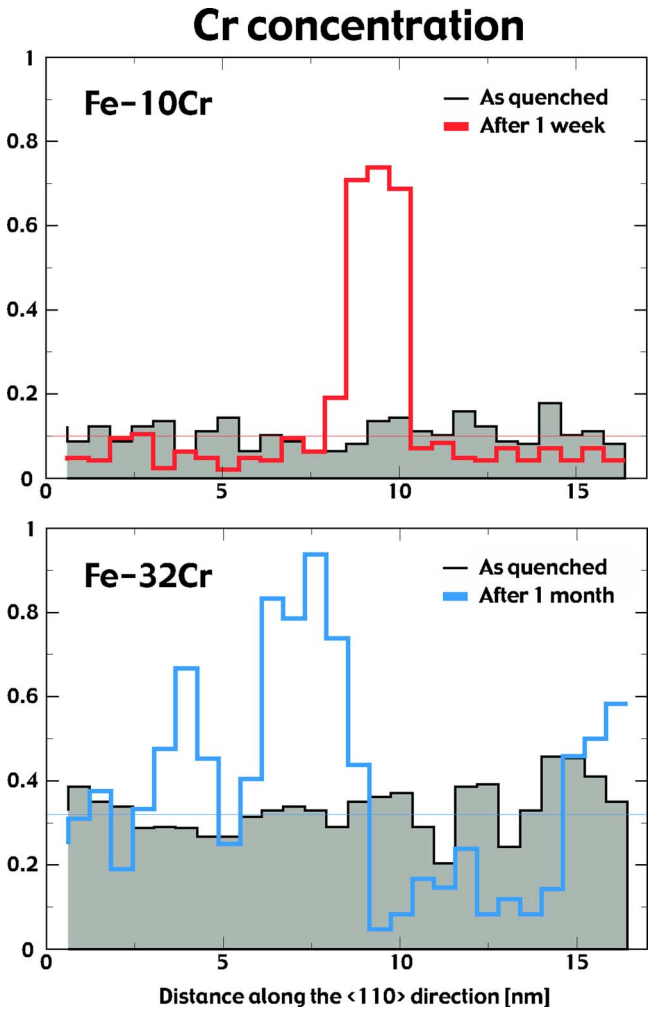

FIG. 5. (Color online) Cr concentration profile along the ⟨110⟩ direction in initially random Fe-10Cr and Fe-32Cr aged at 740 K during one week and one month, respectively. The potential fitted to VASP mixing enthalpy (potential A) was used in the simulation.

VI. CONCLUSIONS

We conclude that the two-band second-moment model of Fe-Cr here developed is able to reproduce thermodynamic properties of the alloy over the whole range of Cr concentration, including solubility limits and formation of the α-prime phase under thermal aging. For this purpose, it was found sufficient to fit the mixed *s*-electron density functional to the mixing enthalpy. Our method enables one to model transition metal alloys with finite miscibility gaps in a quantitative manner. It will be instrumental in further studies of microstructure evolution in ferritic steels under thermal aging and irradiation conditions.

ACKNOWLEDGMENTS

The authors wish to thank Graeme Ackland, Vassilis Pontikis, and Igor Abrikosov for enlightening discussions. This work was funded by Svensk Kärnbränslehantering AB, the European Commission, and Vetenskapsrådet.

[1] M. S. Daw and M. I. Baskes, Phys. Rev. B **29**, 6443 (1984).
[2] M. Finnis and J. Sinclair, Philos. Mag. A **50**, 45 (1984).
[3] A. Voter, in *Intermetallic Compounds, Principles*, edited by J. H. Westbrook and R. L. Fleischer (Wiley, New York 1995), vol. 1.
[4] S. M. Foiles, M. I. Baskes, and M. S. Daw, Phys. Rev. B **33**, 7983 (1986).
[5] G. J. Ackland and V. Vitek, Phys. Rev. B **41**, 10324 (1990).
[6] E. M. Lopasso, M. Caro, A. Caro, and P. Turchi, Phys. Rev. B **68**, 214205 (2003).
[7] J. Wallenius, P. Olsson, C. Lagerstedt, N. Sandberg, R. Chakarova, and V. Pontikis, Phys. Rev. B **69**, 094103 (2004).
[8] F. Cyrot-Lackmann, J. Phys. Chem. Solids **29**, 1235 (1968).

[9] A. E. Carlsson and N. W. Ashcroft, Phys. Rev. B **27**, 2101 (1983).
[10] D. Pettifor, J. Phys. F: Met. Phys. **8**, 219 (1978).
[11] R. Fischer, E. Dulis, and K. Carroll, Trans. AIME **197**, 690 (1953).
[12] S. Brenner, M. Miller, and W. Soffa, Scr. Metall. **16**, 831 (1982).
[13] J. Hyde, A. Cerezo, M. Miller, and G. Smith, Appl. Surf. Sci. **76/77**, 233 (1994).
[14] J. Hyde, M. Miller, A. Cerezo, and G. Smith, Appl. Surf. Sci. **87/88**, 311 (1995).
[15] M. Mathon, Y. Carlan, G. Geoffrey, X. Averty, A. Alamo, and C. de Novion, J. Nucl. Mater. **312**, 236 (2003).
[16] G. J. Ackland and S. K. Reed, Phys. Rev. B **67**, 174108 (2003).
[17] G. Ackland, M. Mendelev, D. Srolovitz, S. Han, and A. Barashev, J. Phys.: Condens. Matter **16**, S2629 (2004).
[18] P. Olsson, I. Abrikosov, L. Vitos, and J. Wallenius, J. Nucl. Mater. **321**, 84 (2003).
[19] F. Willaime, C. C. Fu, M. C. Marinica and J. Dalla Torre, Nucl. Instrum. Methods Phys. Res. B **92**, 228 (2005).
[20] J. Wallenius, P. Olsson, and C. Lagerstedt, Nucl. Instrum. Methods Phys. Res. B **228**, 122 (2005).
[21] G. Kresse and D. Joubert, Phys. Rev. B **59**, 1758 (1999).
[22] P. E. Blöchl, Phys. Rev. B **50**, 17953 (1994).
[23] C. Domain, P. Olsson, and J. Wallenius Phys. Rev. B (to be published).
[24] W. Pearson, *A Handbook of Lattice Spacings and Structures of Metals and Alloys* (Pergamon Press, New York, 1958).
[25] K. Katahara, M. Nimalendran, M. Manghnani, and E. Fischer, J. Phys. F: Met. Phys. **9**, 2167 (1979).
[26] G. Loper, L. Smedskjaer, M. Chason, and R. Siegel, in *Positron Annihilation*, edited by P. Jain, R. Singru, and K. Gopinathan (World Scientific, Singapore, 1985), p. 461.
[27] H. Schultz, Mater. Sci. Eng., A **141**, 149 (1991).
[28] E. Clementi and C. Roetti, At. Data Nucl. Data Tables **14**, 197–211 (1974).
[29] O. K. Andersen and T. Saha-Dasgupta, Phys. Rev. B **62**, R16219 (2000).
[30] P. Olsson, I. Abrikosov, and J. Wallenius Phys. Rev. B (to be published).
[31] B. Györffy, Phys. Rev. B **5**, 2382 (1972).
[32] A. E.Kissavos, S. Simak, P. Olsson, L. Vitos, and I. A. Abrikosov, Comput. Mater. Sci. **35** 1 (2006).
[33] C. Becquart, K. Decker, C. Domain, J. Ruste, Y. Souffez, J. Turbatte, and J. V. Duysen, Radiat. Eff. Defects Solids **142**, 9 (1997).
[34] S. Burke, R. Cywinski, J. Davis, and B. Rainford, J. Phys. F: Met. Phys. **13**, 451 (1983).
[35] R. Hafner, D. Spisak, R. Lorenz, and J. Hafner, J. Phys.: Condens. Matter **13**, L239 (2001).
[36] W. Young and E. Elcock, Proc. Phys. Soc. London **89**, 75 (1966).